Vibration-based ice monitoring of composite blades using artificial neural networks under different icing conditions

Jan Wittig[a,b,1,*], Georgios Tzortzinis[a,c], Niels Modler[a], Angelos Filippatos[d]

[a]*Institute of Lightweight Engineering and Polymer Technology, Technische Universität Dresden, 01307, Dresden, Germany*
[b]*Department of Engineering Science, University of Oxford, OX1 3PJ Oxford, United Kingdom*
[c]*Dresden Center for Intelligent Materials (DCIM), Technische Universität Dresden, 01307 Dresden, Germany*
[d]*Machine Design Laboratory, Department of Mechanical Engineering & Aeronautics, University of Patras, 26504 Patras, Greece*

Abstract

Cold climates pose significant challenges for wind turbines, primarily due to icing complications that influence electrical energy production. Precise methods are needed to identify and predict ice distribution on blades. Thus, enhancing prediction of ice accumulation based on the blade's frequency response. The study involves using glass fiber reinforced plastic composite rotor blades equipped with actuators and accelerometers to measure the response of the blade subjected to icing, with a total of 1700 measurements. Small-scale icing experiments are conducted inside a climate chamber at temperatures from −10 °C to −20 °C with seven icing distribution profiles on the blades. The gathered data are analyzed for the effects of icing on the frequency response of the blades. Additionally, we propose the use of optimized artificial neural networks to predict the accumulated ice thickness on rotor blades with a weighted mean absolute percentage error of 5.1 %, and ice volume and ice mass with an error of 5.7 %, based on the frequency response. Overall, this paper investigates the relation between icing, with regard to ice mass, ice location, and ambient temperature, and frequency response of wind turbine blades, along with proposing a high-performance method for ice detection and monitoring during operation.

Keywords:
Ice Prediction, Machine Learning, Frequency Analysis, Icing Experiments, Rotor Blade, Signal Processing

1. Introduction

Renewable energy sources have become increasingly important as the world has become more aware of the need to reduce greenhouse gas emissions. As such an energy resource, wind energy can be used to generate electricity, providing a clean source that does not emit greenhouse gases, thereby contributing to the mitigation of climate change. The deployment and installation of wind turbines (WTs) to harvest wind energy are increasing worldwide to reduce and substitute electrical energy generation from fossil fuels. WTs and wind farms with a total capacity of 825 GW [1] in 2021 are located all over the world, including in cold climate regions.

While cold climate regions offer significant benefits for wind energy harvesting due to the higher air densities, these areas present unique challenges for WTs, particularly due to harsh environmental conditions

*Corresponding author
Email address: jan.wittig@eng.ox.ac.uk (Jan Wittig)
[1]Present affiliation: Department of Engineering Science, University of Oxford

like icing. Icing can impair blade aerodynamics and, during severe weather scenarios, cause a substantial decrease in energy production or even lead to a total shutdown [2].

The expected surge in installed wind power capacity in cold climate regions, projected to increase by 224 GW by 2025, emphasizes the growing importance power loss due to icing [3]. The impact of such icing can be so severe that it results in up to 20 % of annual energy production loss for WTs [4]. This points to the critical necessity of ice detection, prevention, and removal methods to minimize power loss. If blades get heavily iced, costly deicing techniques must be implemented, creating a significant financial burden for operators [5]. This highlights the interconnected challenges and the need for effective ice prediction strategies to harness wind power optimally in cold climate regions.

Several researchers have investigated ice detection and prediction on blades by using artificial neural networks (ANNs). Li et al. [6] investigated the ice prediction on a 2 kW WT blade in standstill conditions, employing modal frequencies as input parameters for an ANN. The results showed that the ANN could classify the ice mass and distribution along the blade within in three discrete define zones. Gantasala et al. [7] also used natural frequencies to predict ice mass and its location along a WT blade as a classification, which was divided into three zones. A change of mass and stiffness due to the icing caused a shift in natural frequencies, which the ANN was able to detect and interpret. Gantasala et al. conducted an experimental verification using a cantilever beam, where the ANN with finite element method (FEM) generated data was tested. Furthermore, an ANN was trained on simulated FEM data of a 2 MW WT blade and was able to predict the ice mass and distribution on a rotating blade. In a further work, Gantasala et al. [8] demonstrated the successful application of an ANN to predict the ice mass and ice location of within three zone along a 1 kW blade. The data were gathered experimentally by using an excitation signal up to 200 Hz and accelerometers for monitoring the response. As input data, the obtained natural frequencies from the experiments were given into the ANN. Furthermore, the ANN was deployed with decent results on simulated data of a 5 MW stationary WT blade.

Systems for ice detection applications, such as BLADEcontrol [6] or Wölfel IDD.Blade [9], are commercially available. These control systems monitor vibrations of the blade, and after signal processing, obtains the natural frequencies. From the changing natural frequencies of the blade, the accumulated ice can be detected. The comprehensive exploration of how ice mass, ice distribution, and ambient temperature affect a composite blade's frequency response, and the subsequent prediction of these properties, remains an under-researched area. Filippatos et al. [10, 11] have recently conducted research into the effects of ice on the frequency response of small-scale composite blades, focusing on the relationship between the ice mass and its placement on the blade's frequency response. However, to detect patterns and correlations, additional exploration of the ice's impact on the frequency response is beneficial. The research, including ANNs with regression, to predict the ice thickness and mass based on the blade's frequency response could enhance predictive capabilities regarding ice accumulation on WTs blades.

Furthermore, there is a lack of a methodology for predicting the ice distribution across the blade's length, as the previous investigations only focused on ice detection of specific zones along the blade. To the author's knowledge, no research has been published on predicting, based on the blade's frequency response, the ice distribution across a blade.

2. Methodology for enhancing predictive capabilities

For enhancing predictive capabilities, a methodology with five steps is applied, shown in Figure 1, starting with the manufacturing of the blades, see Section 3.1. Each blade is equipped with single macro fiber composite (MFC) actuator, accelerometer, and temperature sensor [12]. This enables to record the blade's response to ice accumulation and ambient temperature.

For the execution of the icing experiments, the blades are mounted in a test rig. These experiments are carried out under three different temperature conditions: $-10\,°C$, $-15\,°C$ and $-20\,°C$, described in Section 3.3, each of which simulates different cold weather situations that are encountered by WTs blades in real-world settings. Furthermore, the icing experiments incorporate seven configurations of ice distribution, simulating the random complex nature of icing on blades.

The blades' responses during the icing experiments are captured by the accelerometers. This raw data are then processed, in Section 3.3, using signal processing methodologies using the fast Fourier transform (FFT) for analyzing the frequency components of the collected time-series data.

Following the initial signal processing, further transformations of the data are performed to prepare the data for the training of ANNs. This step involves data scaling, preparation, and transformation in Section 4.1.

Finally, the processed and transformed data are used to train the ANNs in Section 4.3. Once trained, these ANNs are used to predict various aspects of ice accumulation on the blades, including ice thickness along the blade, ice volume, and mass of accumulated ice. These predictions results detect ice with high performance on WT blades. The main contributions of are:

1. Characterization of influence of ice accumulation on a composite blade's frequency response.
2. Ice prediction, in terms of ice distribution, volume and mass based on the blade's frequency response.

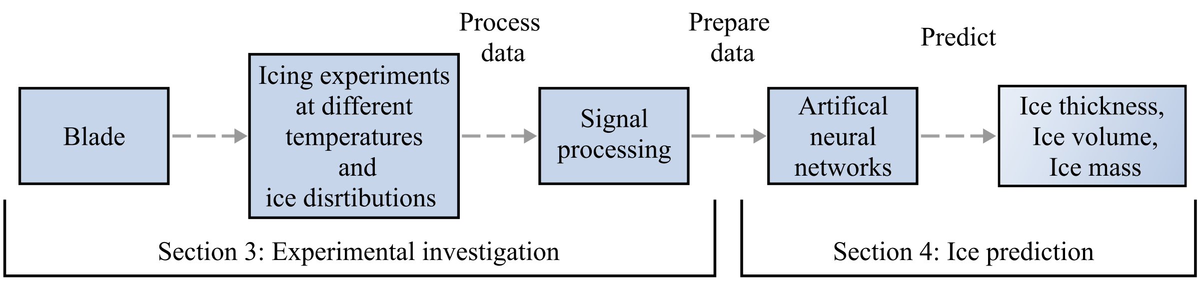

Figure 1: Flowchart of the proposed methodology, consisting of five steps.

3. Experimental Investigation - Impact of icing on composite blades

3.1. Materials

A symmetric glass fiber-reinforced plastic (GFRP) layup consisting of four plies is selected, utilizing a $[0, 90]_S$ glass fiber cross-ply configuration, with orthotropic material properties with laminate thickness of 1 mm . The laminate is made up of woven unidirectional (UD) glass fabrics [13] with an area weight of $220\,\mathrm{g\,m^{-2}}$. The epoxy resin RIMR-135, in conjunction with the accelerator RIMH-137, is supplied by the manufacturer HEIXON [14]. The mechanical properties of resin and glass fiber can be found in Table 1. The blade shells are fabricated utilizing a vacuum assisted resin infusion (VARI) process. The identification and prediction of ice accumulation are contingent upon the frequency spectrum of the blade. To elicit a response from the blades, each blade is excited using a M2814-P1 MFC actuator. The response from the MFC actuator's excitation is measured via a type ADXL321 accelerometer, utilizing a capacitance-based measurement principle [18], and is embedded on a board measuring acceleration in two axes (X,Y). In addition, the accelerometer board is bonded to the blade cover, composed of 3D printed GreenTEC-Pro material, and embedded with two-component epoxy for environmental protection. For enhanced monitoring, the blades are augmented with internally bonded analog humidity-temperature sensor SHT31-ARP [19].

Table 1: Overview of the mechanical properties of the used materials in the blade.

Property	Fiber (glass fiber) [15]	Matrix (RIMR 135) [14, 15]	3D-filament [16, 17]
Young's modulus (MPa)	73000	3000	4300
Shear modulus (MPa)	29920	1110	1593
Density ($\mathrm{g\,cm^{-3}}$)	2.504	1.190	1.350
Poisson's ratio ν_{12}	0.22	0.35	0.35

The sensor, integrated on a breakout board, offers an operational temperature range from −40 °C to 125 °C with an accuracy tolerance of ±0.3 °C. The manufactured blades, equipped with actuators and sensors, are shown in Figure 2.

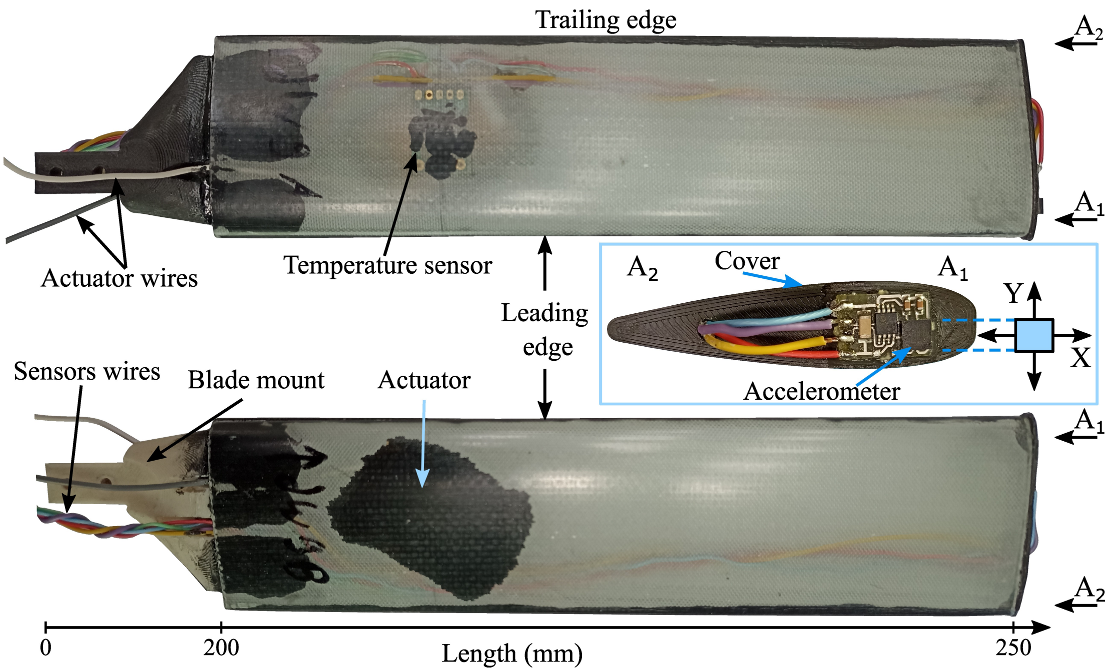

Figure 2: Pictures of the finished blades equipped with temperature sensors, accelerometers, and actuators. The measurement directions of the accelerometer are denoted by X and Y.

3.2. Experimental and instrumental setup

To investigate the effects of icing on the blade's frequency response, the blade icing (BLICE) test rig was used [11]. This test rig provides a variety of opportunities for exploring the impact of icing on blades. The test rig comprises various components, including a climate chamber, data acquisition devices, an electric motor, and a water supply system with a nozzle set. The components of the BLICE test rig, shown in Figure 3, are placed inside a climate chamber (1). A containment (11) encloses the icing zone and protects the climate chamber from the impact of detaching ice. In the center of the containment, the motor shaft flange is located (3), where the blades (2) are mounted to the shaft. The BLICE test rig's servo motor (15) is

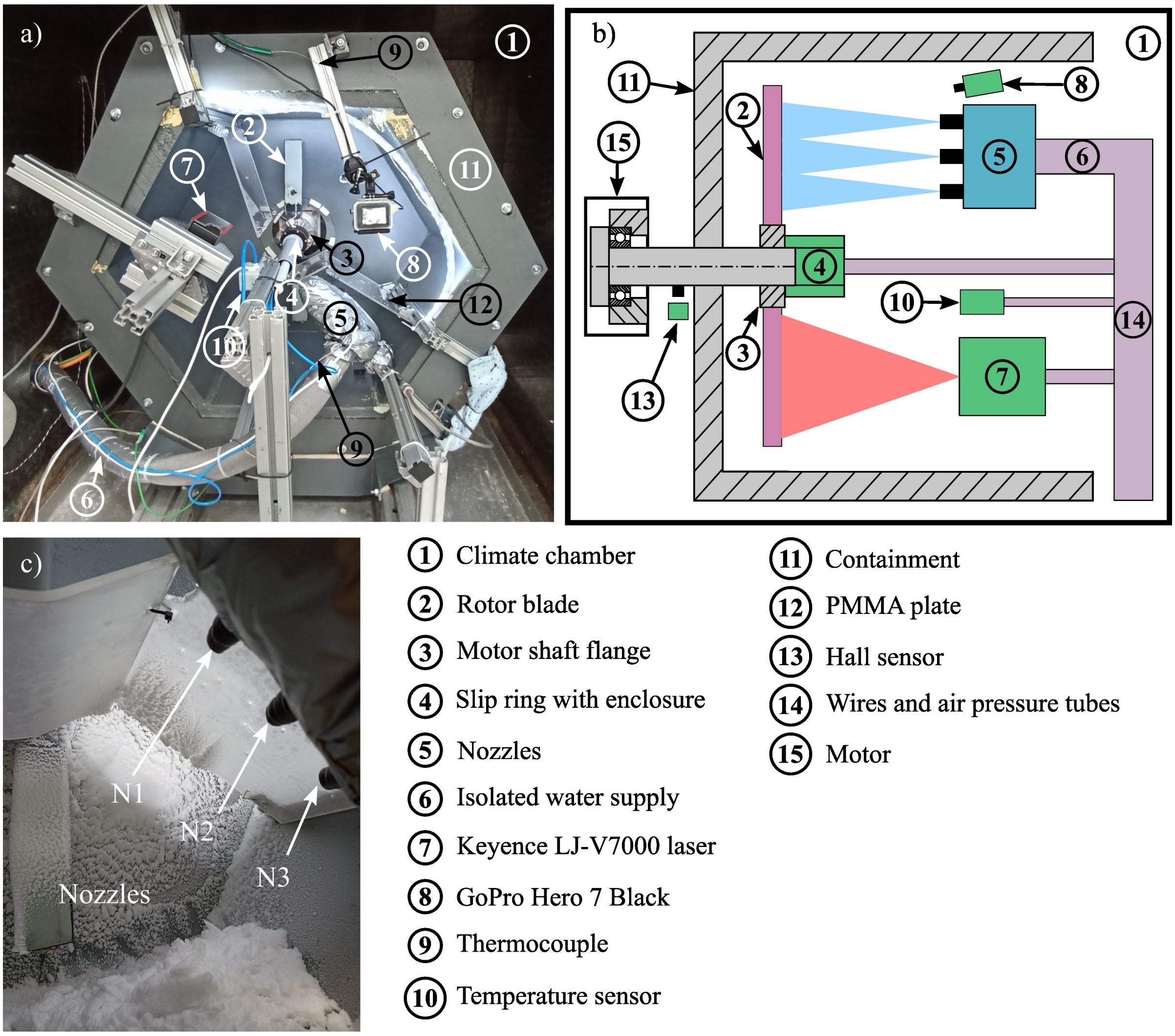

Figure 3: a) Top view of the BLICE test rig with its components. b) The schematic top view of the used components inside the BLICE test rig for the experiments. c) The nozzle N1 sprays to the root area of the blade, the nozzle N2 to the middle area, and the nozzle N3 to the tip area.

situated behind the containment. The rotational speed of the shaft and the position of the blade are monitored with a Hall sensor (13). The ice on the blades inside the climate chamber is generated by spraying water from the nozzles (5). The spraying unit consists of three air-driven nozzles (N1, N2, N3) radially arranged from the shaft towards the contaminant. Each nozzle with its spray volume is individually adjustable by air pressure and internal nozzle diameter. The air pressure for the nozzles is set to 3 bar. To monitor the temperature, two thermocouples and one temperature sensor (10) are placed. The test rig includes a Keyence LJ-V7000 profile line laser (7) to measure the accumulated ice thickness, which measures a finite number of points along a line, spanning the entire blade length. Additionally, the icing experiments can be recorded with an installed GoPro Hero-7-Black camera (8), which is housed within an enclosure for environmental protection.

The experimental modal analysis (EMA) is conducted, via two National Instruments measuring cards of the type USB-6212, by exciting with the actuator and measuring its response with the integrated accelerometer. The analyzed frequency range is defined from 0 Hz to 2000 Hz. To obtain a sufficient frequency spectrum resolution, the sampling rate of the second card is set to 10000 Hz [20].

3.3. Design of experiments and experimental modal analysis

For each temperature −10 °C, −15 °C, and −20 °C a corresponding testing campaign is conducted. The BLICE test rig is equipped with three nozzles, allowing seven possible nozzle configurations, each denoted by a distinct digit following

$$\text{nozzle configuration} = [\text{N1 N2 N3}]\,, \tag{1}$$

where N1 represents the root nozzle, N2 the middle nozzle, and N3 the tip nozzle. The experiments carried out for a specific nozzle configuration are referred to as measuring series. Thus, each measurement campaign comprises all seven possible measuring series. A measuring series itself consists of multiple single EMAs and profile line laser measurements. To obtain a sufficient amount of data of the increasing ice accumulation on the blade, at least 40 single measurements are carried out for each measurement series. Thus, from both blades and considering all the measuring campaigns and series, a total of 1700 valid single measurements are obtained. A single measurement conducts an EMA and a laser measurement with a duration of 40 s at a rotor speed of 100 RPM. The first measurement is always performed without icing to acquire an ice-free reference measurement. During subsequent measurements, the nozzles are closed to ensure accurate measurement of the accumulated ice. Between each single measurement, the corresponding nozzle configuration is opened, and blades are iced for 3 min, allowing incremental ice accumulation to be achieved and recorded. An overview of the measuring campaigns with the corresponding measurement series is shown in Table 2. With increasing distance along the blade to the rotational axis, the rotational velocity increases. Accordingly, the spray volumes of the nozzles are adjusted to gradually increase from the root to the tip area to ensure a uniform distribution of ice. Preliminary tests showed an optimal spray volume range of water between 3 g min^{-1} and 6 g min^{-1} for icing the blades. Therefore, prior to each measurement series, the nozzles are calibrated to ensure a similar spray volume across the measurement series, with N1 at 4.0 ± 0.2 g min^{-1}, N2 at 4.5 ± 0.2 g min^{-1}, and N3 at 5.0 ± 0.2 g min^{-1}.

Table 2: Measuring campaigns of the icing experiments. An open nozzle is indicated by 1 and a closed nozzle by 0.

Measuring campaign for each temperature (°C)		Measuring series for each nozzle configuration		Single measurements
		[001]	⟶	1...40
		[010]	⟶	1...40
		[011]	⟶	1...40
−10, −15, −20	⟶	[100]	⟶	1...40
		[101]	⟶	1...40
		[110]	⟶	1...40
		[111]	⟶	1...40

The principle procedure of the EMA consists of inputting an excitation signal for an actuator to induce a vibration of the blade and measure its response by an accelerometer. The excitation is defined as a quadratic chirp signal starting from 0.1 Hz to 2000 Hz in a time range of 40 s, shown in Figure 4. The embedded accelerometers, on the cover of the blades, measure the excited out-of-plane vibrations of the blades as a voltage signal. The blades' in-plane measurement orientation, which demonstrates a highly noisy signal during rotation, is omitted from subsequent analysis due to its lack of valuable information. Consequently, only the out-of-plane blade orientation is employed for assessing the blades' frequency responses. The accelerometers' voltage signals, when in a horizontally stationary position, exhibit 2.5 V displayed in Figure 4. Slight differences in voltage offset levels among the blades are due to minor discrepancies in the bonded accelerometers. From the accelerometer's response, vibrations of the blades are visible, especially at higher frequencies with increasing time. Subsequently, the accelerometer's voltage signal undergoes transformation via a FFT. The resulting FFT-transformed accelerometer signal presents a noisy frequency spectrum. To acquire a defined frequency response spectrum, a moving average is applied to the Fourier-transformed data. The frequency response of the moving average, representing an average of the frequency amplitude, is utilized for further data processing. The FFT data outcomes and the consequent frequency response of the blades are depicted in Figure 4.

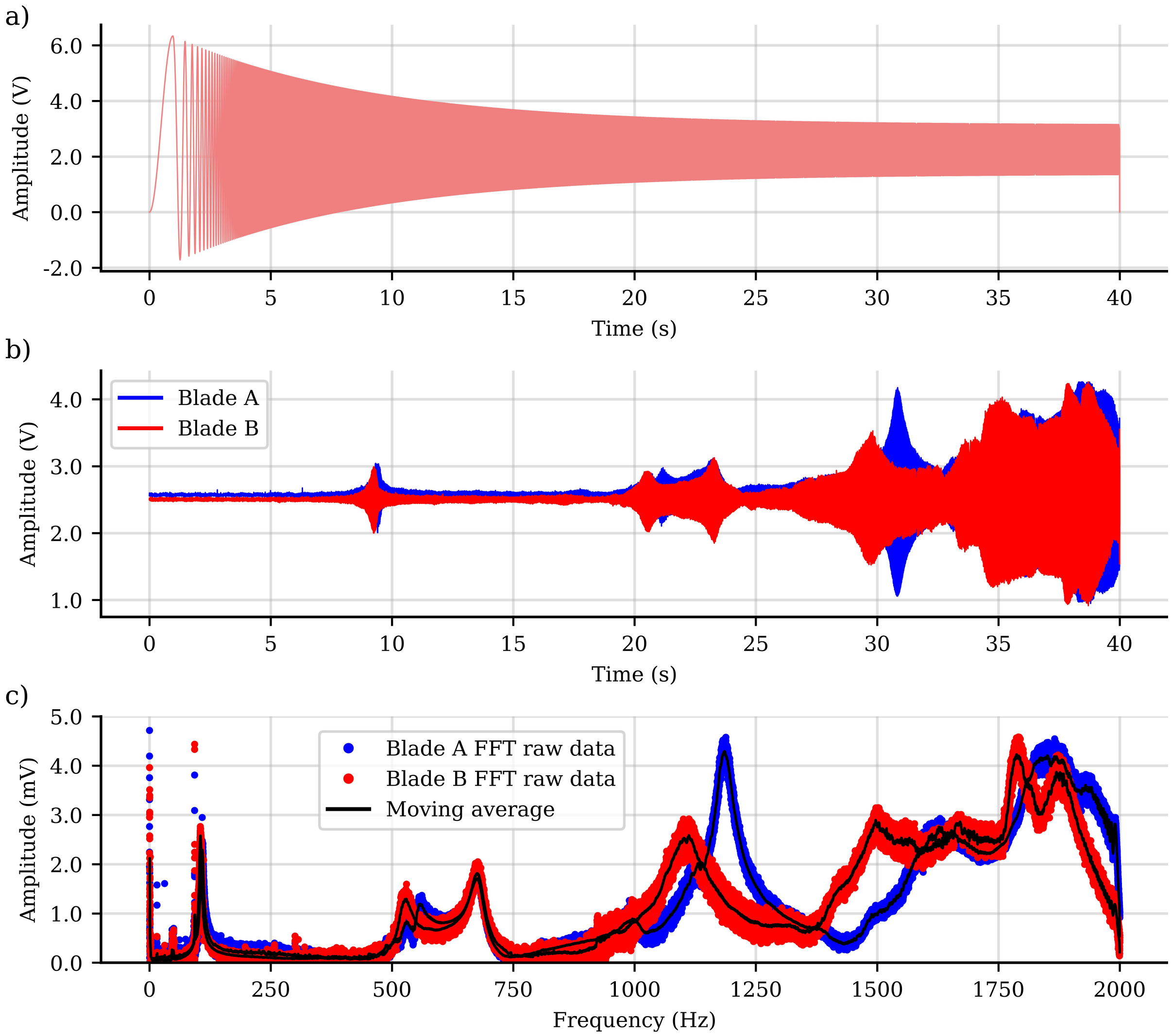

Figure 4: a) The excitation signal for the actuator. b) The responses of the excited blades measured by the accelerometers. c) The frequency responses of the blades obtained from the FFT, along with the applied moving averages. The EMA was conducted at a rotational speed of 100 RPM.

3.4. Determination of ice thickness, ice volume, and ice shape

Throughout the EMA, the laser measures with a sampling rate of 1000 Hz, capturing the blade surface measurements. The Keyence LJ-V7000 laser gauges the distance between the measuring object and the laser along a predefined profile line. Firstly, the boundaries of each blade revolution within the data are identified and extracted. As a result, the extracted data represents a continuous measurement of one revolution. To identify the position of each data point within the extracted data for one revolution, a discretized equation is defined. To this end, the equation of the circle circumference is discretized into finite steps. Using the acquired number β, which signifies the number of discrete profile lines of the measured laser lines for one revolution within the data, and the discretized radius r, the laser measurement data at any discrete point can be defined following

$$P_{data}(\alpha, \beta, r) = \frac{2\pi\alpha r}{\beta}, \tag{2}$$

with $\alpha \in \{0, \ldots, \beta\}$ denoting a single laser profile line within one revolution. In the next step, the data are transformed from a polar-based coordinate system into a Cartesian-based coordinate system under the consideration of the previously discrete profile lines Equation (2). This conversion results in the following transformation equations

$$x_{trans} = cos\left(\frac{2\pi\alpha r}{\beta}\right) \tag{3}$$

$$y_{trans} = sin\left(\frac{2\pi\alpha r}{\beta}\right). \tag{4}$$

Utilizing Equations (3) and (4), the laser data are transformed into a Cartesian coordinate system for further processing. The transformed point clouds of both blades for one extracted revolution are shown in Figure 5.

Based on the processed laser data of the single measurements, the ice shape can be derived as a single point cloud by combining two point clouds from two single measurements. The initial single measurement, always taken without ice, serves as the reference point cloud. The second point cloud corresponds to a single

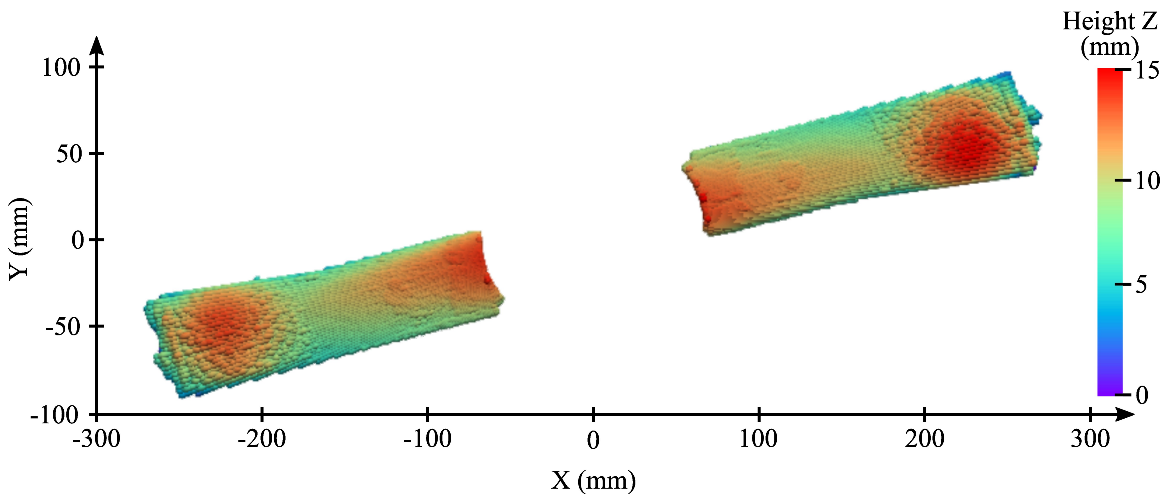

Figure 5: Point clouds of the transformed laser data of the blades. The displayed data are recorded at −15 °C at 100 RPM.

measurement, which can involve any measurement with ice accumulation on the blade. Thus, both point clouds can be merged into one, from which the shape and volume can be determined. The space between the reference and any arbitrary point cloud represents the accumulated ice on the blade. The actual ice thickness is determined by subtracting any individual measurements from the reference measurements and identifying it as the height difference between the measured profile lines and the reference measurement. The icing experiments showed that the ice distribution across the blade width is similar. Therefore, to simplify the ice thickness determination along the blade length only the middle lines along the blade of both point clouds are subtracted, yielding the ice thickness.

The stacked point cloud can be meshed by applying an implemented triangulation algorithm. For this purpose, the Delaunay 3D algorithm from PyVista [21] is employed. Thus, the stacked point cloud is meshed to obtain an enclosed ice volume and shape, exemplarily shown in Figure 6.

Additionally, the enclosed ice volume can be determined from the stacked point cloud. The enclosed volume of point clouds is calculated by MATLAB's boundary function. In addition, the ice volume is subdivided into three sub-volumes V1, V2 and V3 along the blade for each nozzle. Since the blade root is transformed to the coordinate origin, the sub-volumes are divided along the blade length, ranging from 0 mm – 67 mm for V1, 67 mm – 133 mm for V2 and 133 mm – 200 mm for V3, respectively.

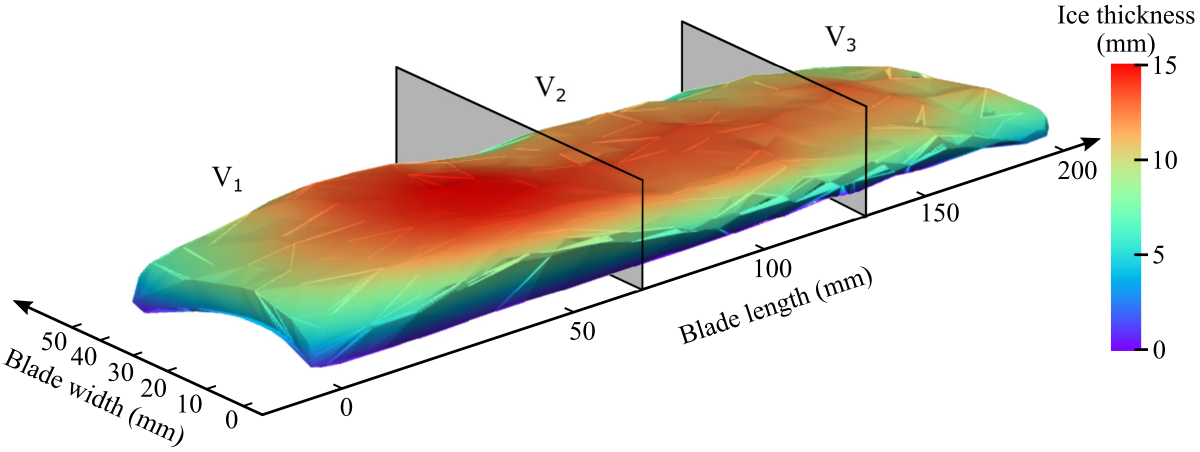

Figure 6: The ice volume and its sub-volumes from the meshed point cloud of Blade A at −15 °C in a [111] nozzle configuration.

3.5. *Analysis of ice density*

After every measuring series (seven measurement values), the accumulated ice on the blade is scraped off and weighed, allowing for the determination of the ice mass, shown in Table 3.

The deviation of the calculated densities at −10 °C shows the largest discrepancy. This discrepancy is believed to result from the imprecise ice mass measurement method and errors in the calculated volumes from the point clouds. Additionally, the deviations of the calculated ice density between both blades are minor, which shows equally distributed ice mass across both blades in conjunction with the measured ice mass. In conclusion, the results show a linearly decreasing ice density and increasing ice volume with decreasing temperatures.

The obtained ice densities for the temperatures −10 °C, −15 °C and −20 °C show similar ice densities and ice appearance as described in the literature [22]. At temperatures around −10 °C, the ice appearance is a blend of glaze and rime ice type. The water droplets freeze not necessarily upon impact, and the water droplet can unify and grow over time, resulting in a mixture of glaze and rime ice. At lower temperatures at

−15 °C and −20 °C, the ice appears as a rime ice type with significantly more volume. It is believed that the water droplets at these temperatures freeze upon impact on the blade, preventing uniform ice growth. Thus, more air voids are contained within the ice, leading to larger ice volumes and lower densities.

Table 3: Ice densities of the accumulated ice, at a speed of 100 RPM on the blades, for different temperatures.

Temperature (°C)	−10		−15		−20	
Blade	A	B	A	B	A	B
Max. density ($g\,cm^{-3}$)	0.92	0.93	0.64	0.62	0.46	0.50
Min. density ($g\,cm^{-3}$)	0.56	0.57	0.45	0.45	0.33	0.34
Avg. density ($g\,cm^{-3}$)	0.75	0.78	0.50	0.50	0.38	0.40

3.6. Experimental results

Influence of temperature on the frequency response

For investigating the influence of temperature, a temperature range from 30 °C down to −20 °C with 5 °C steps is chosen. The results of the temperature influence on the frequency response are shown in Figure 7. One notable observation is a discernible shift in eigenfrequencies towards higher frequency values

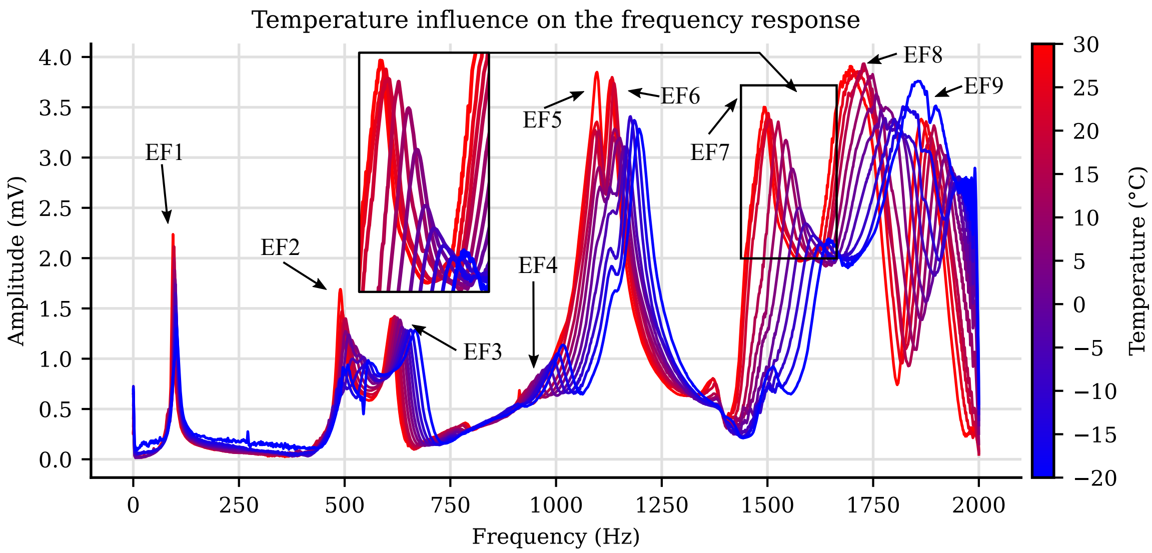

Figure 7: Temperature influence on the frequency response of Blade A in the temperature range from 30 °C to −20 °C in 5 °C steps at 0 RPM. The eigenfrequencies are denoted by EF.

as the temperature decreases. Additionally, at higher frequencies above 500 Hz, an increasing influence of the temperature on the frequency responses is visible, resulting in increasing deviation between eigenfrequencies. With decreasing temperatures, the amplitude of the frequency response decreases. The change in frequencies is attributed to the increased stiffness of the GFRP blades [23]. Analogous findings concerning the increased frequency with decreasing temperatures of a polyethylene composite beam were reported [24].

Influence of ice mass on the blade's frequency response

With a minimum of 40 valid icing intervals and single measurements for each measuring series, the influence of ice mass can be determined. As an example for illustration, the influence of the ice mass on the frequency responses of the nozzle configuration [010] at $-15\,^{\circ}\mathrm{C}$ is exemplarily shown in Figure 8. The amplitude changes with decreasing frequency amplitude are visible through the transition from reddish to greenish or bluish tones. The impact of accumulated ice mass becomes noticeable in the middle range, leading to deviations in frequency response amplitudes. At higher frequencies, a substantial influence of

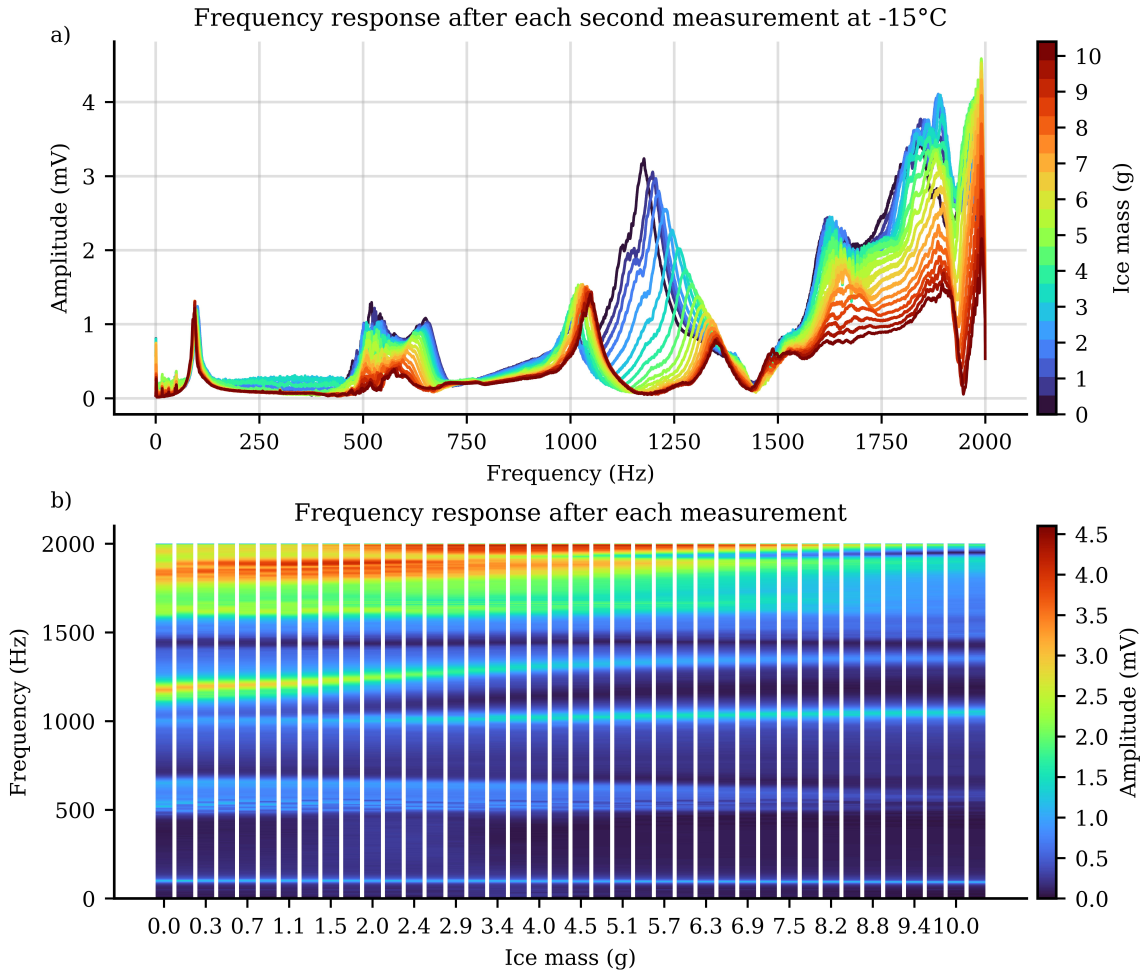

Figure 8: a) Influence of accumulated ice mass on the frequency response of Blade A in the nozzle configuration [010]. b) The frequency responses, visualized with color bars with their amplitudes at certain ice masses.

ice mass is evident, showing a decreasing trend in amplitude with increasing ice mass. Eigenfrequencies are also shifted to lower or higher frequencies, depending on the frequency, due to the ice mass. The correlations between ice mass and frequency response provide valuable information for the ANNs regarding the influence of accumulated ice.

Influence of ice distribution on the frequency response

Ice accumulation and location on turbine blades significantly affect their frequency response. This impact is evident from tests with seven nozzle configurations causing different ice distributions. Such variations lead to distinct frequency responses. For instance, Figure 9 compares blades under similar ice mass conditions, showing that even with a comparable ice mass of around 7 ± 0.3 g, the frequency response varies notably. Lower frequencies up to 500 Hz, show minor differences, but above 500 Hz, the deviations become more pronounced in amplitude and curve progression. Furthermore, the location of the accumulated ice influences the number of eigenfrequencies compared to the reference measurement without ice. Such complex behaviors of frequency changed could be captured by ANNs.

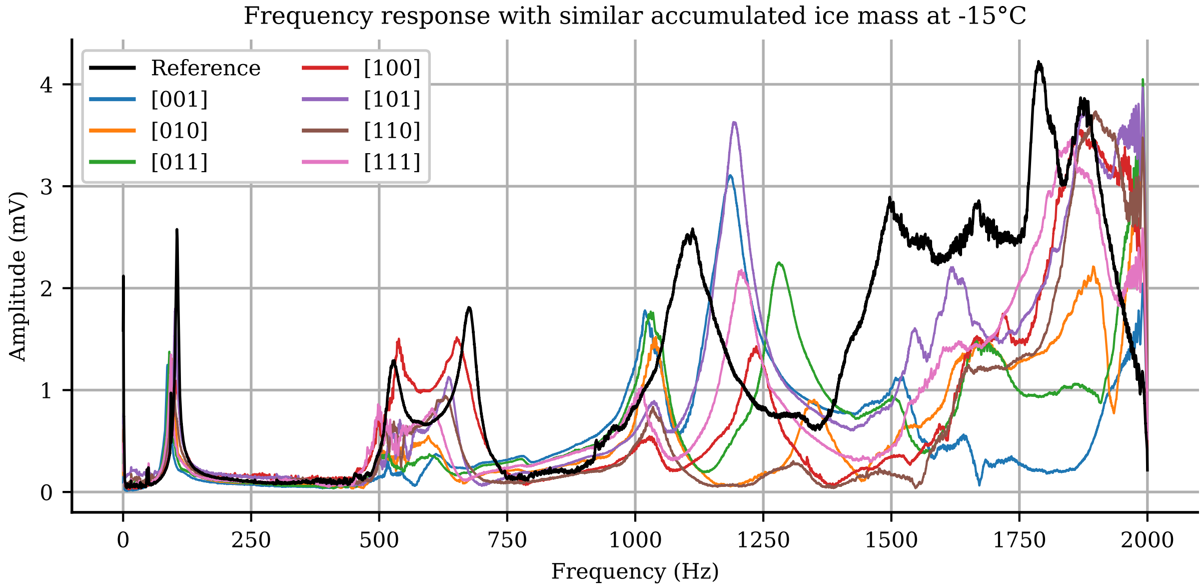

Figure 9: Influence of ice location along on the blades on its frequency responses. The weight of accumulate ice masses is 7 ± 0.3g.

3.7. Discussion of the experimental results

Figure 10 compares the effects of temperature, ice mass, and location on Blade A's frequency response, illustrating these influences through color-coded amplitude bar plots. The ice mass range varies from 0 g to 8 g, in 1-gram increments. Due to slight variations in the spray volume across measuring series, ice accumulation rates and masses differ slightly, within ±0.3 g.

The figure reveals a general decrease in amplitude of frequency responses with increasing ice mass for most nozzle configurations and temperatures, except for one specific configuration [100]. In this case, the amplitude initially increases with ice mass up to 4 g and then decreases with further accumulation. This pattern is thought to be related to ice accumulating near the blade root. Additionally, eigenfrequencies shift to both lower and higher ranges. Additionally, a shift of eigenfrequencies to both lower and higher frequency ranges is evident. At frequencies of around 500 Hz, a shift towards lower frequencies is visible through decreasing slopes of amplitudes with increasing ice mass across all temperature and nozzle configurations. The temperature's effect is also visible, with the color transition from red to green or blue in the plots indicating frequency changes with decreasing temperatures at constant ice mass. In conclusion, each nozzle configuration and its corresponding ice accumulation on the blade exhibit a distinct frequency response, distinguishable from one another at varying temperatures. These patterns provide correlations and information that can be used to train ANNs, predict and monitor icing of the blade.

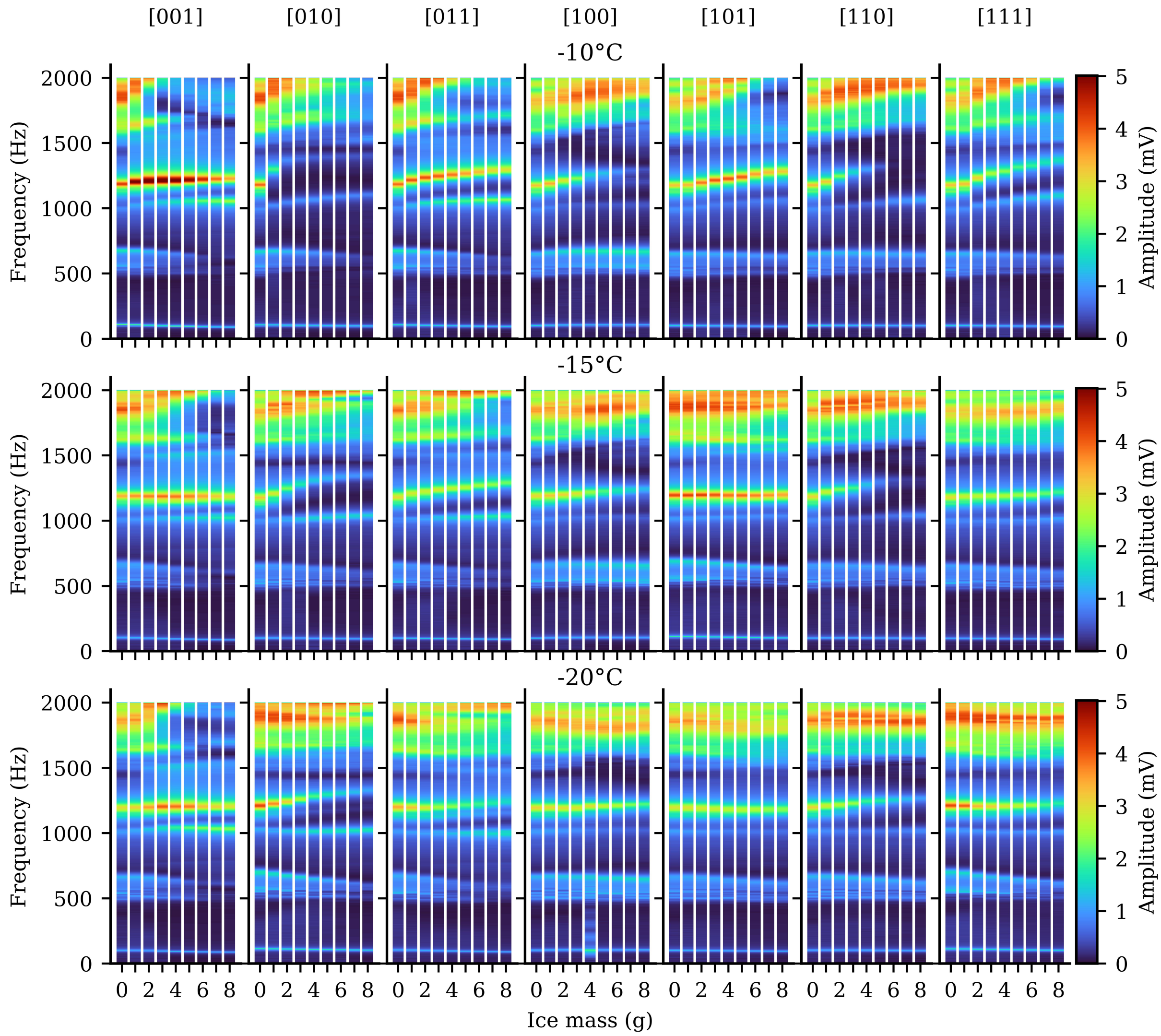

Figure 10: Frequency response of Blade A compared at different temperatures, ice locations and ice masses.

4. Ice prediction using artificial neural networks

Section 3.7 reveals distinct patterns in how ice mass and location at various temperatures affect blade frequency response. ANNs effectively analyze these frequency responses, uncovering complex patterns within the data. This capability enables ANNs to predict ice volume, mass, and thickness.

4.1. Data inspection, scaling, and preparation

Frequency response data can be analyzed using the Pearson correlation coefficient to determine the linear correlation between frequencies [25]. A correlation coefficient of 1 or −1 indicates a strong linear correlation, while 0 shows no correlation. Negative coefficients imply opposite movements in frequency amplitudes [26]. A similar inspection of the frequency data with the Pearson correlation matrix was conducted by Scholz et al. [27]. By observing a concentration of highly correlated data in small areas within the correlation matrix, one can assume that the information in the data can be represented with fewer features by using principal component analysis (PCA), presented in Section 4.2.

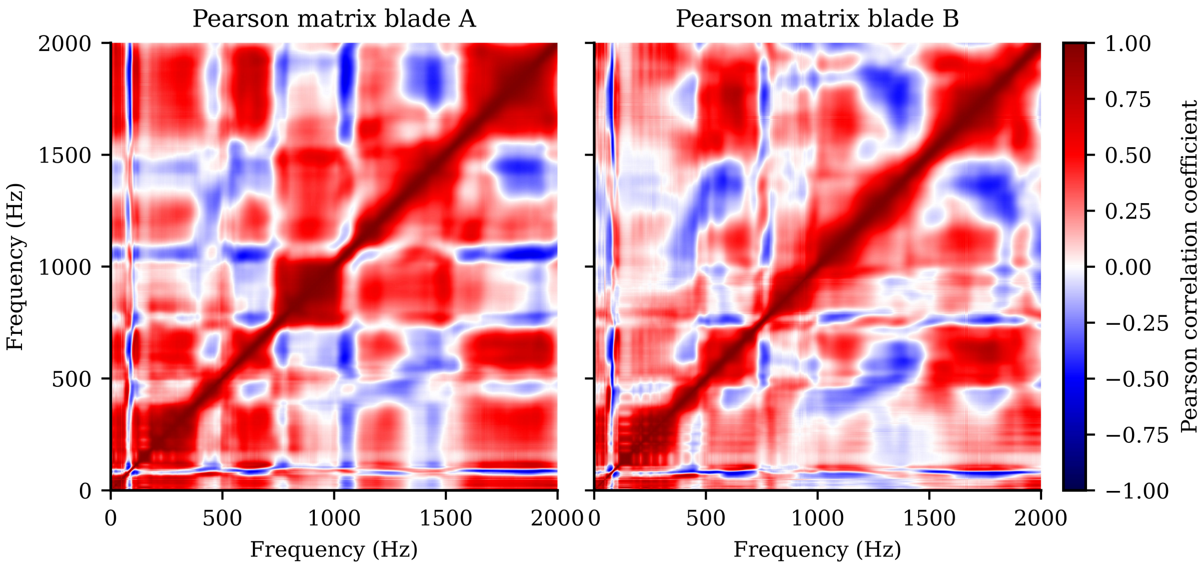

Figure 11: Pearson matrices of the frequency responses from the blades.

Data scaling

Depending on the deployed algorithms, different feature dimensions can influence their performance. The variance along the frequencies shows deviation at some frequencies; therefore, normalization is a suitable scaling technique to prepare the frequency data [28]. The frequency data are normalized by using the library scikit-learn [29].

Ice thickness data preparation

To smooth the uneven ice surface with its ice crystals, a Savitzky-Golay filter [30] is applied to the measured ice thickness. Furthermore, the resolution of the ice thickness is transformed by interpolating the 800 data points with a resolution of 0.5 mm along the blade, resulting in 401 data points to ensure constant data dimension for every measurement.

Dataset preparation

The dataset, containing 1700 samples, is shuffled to eliminate an order of the data and reduce a potential bias of the ANN. The input features of the dataset are represented by the frequency response, and the targets, depending on the prediction, are the features of the ice volume or ice thickness. The dataset is split in a stratified manner into 64 % (1088 samples) of training data, 16 % (272 samples) of validation data, and 20 % (340 samples) of test data. The training and validation data are used during the training of the ANN, and the test data are used to evaluate its performance.

4.2. Principal component analysis on the experimental data

The processed data from the frequency response and ice thickness contain a vast number of data points, which are considered features for the ANN model. In a fully connected ANN, each input feature represents an input neuron of the input layer. However, the dimension of the input data and the targets are too high to handle for an ANN on a computer. To reduce computing time and identify valuable information and patterns, a PCA is applied to the data of the frequency response and ice thickness using the scikit library. PCA is frequently utilized for data dimension reduction or feature extraction. Several researchers [31, 32] applied PCA for dimension reduction on data for training an ANN model to detect or predict ice on a WT blade. Depending on the variance of the data, the number of principal components (PCs) is chosen in such a way that over 99.9 % variance of the raw data is represented. To examine whether the data relate to nonlinear behavior, a kernel principal component analysis (KPCA) is applied. In addition to the linear kernel, radial basis function (RBF), polynomial, and sigmoid kernels are used to compare their performances. The cumulated explained variance is plotted against an increasing number of PCs in Figure 12. The linear kernel approximated with the least amount of PCs the desired 99.9 % explained variance for the frequency response and ice thickness, as shown in Table 4. Therefore, the KPCA is applied with a linear kernel which is equal to the default PCA.

Table 4: Dimensions of the data before and after applying PCA. The explained PCA variance represents the variance of the dataset.

Data state	Data dimensions		
	Ice volume	Frequency	Ice thickness
Raw	3	80000	401
PCs	-	40	10
PCA variance	-	99.9 %	99.9 %

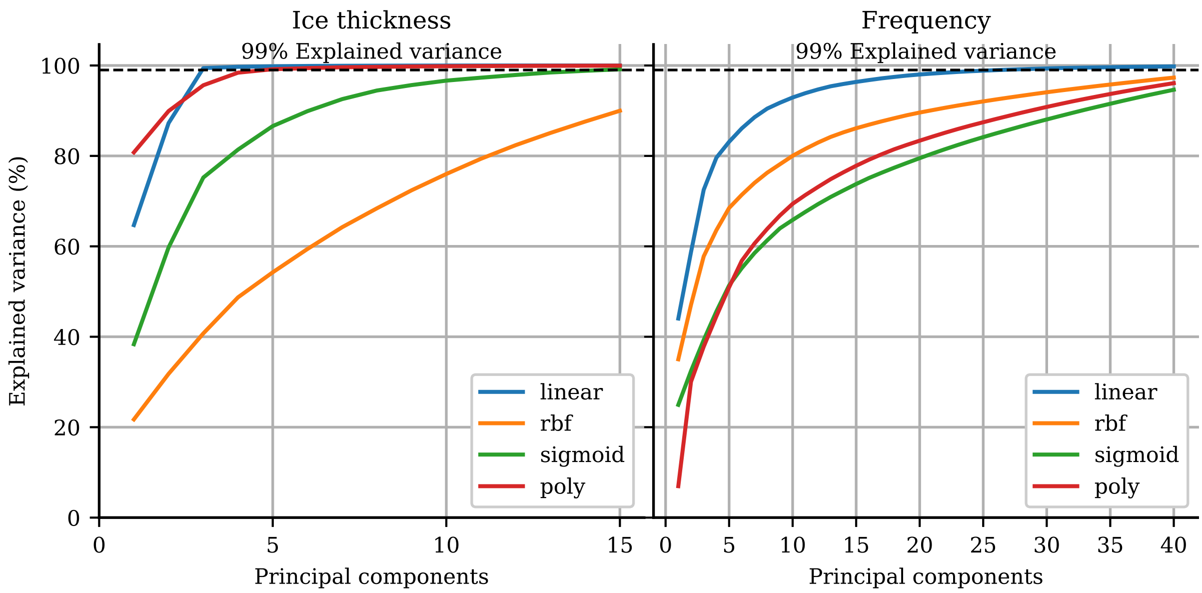

Figure 12: Explained variance of the dataset is plotted over the principal components with different kernels.

4.3. Training and optimization of artificial neural networks

The thickness and volume of ice are predicted through regression tasks utilizing fully connected ANNs from the library TensorFlow [33]. The flowchart, shown in Figure 13, illustrates the procedure to obtain the prediction target values. In the first step, the data are fed into the ANN. Depending on the type of target value, the predictions of the ANN are the final numeric results for the ice volume or PCs for ice thickness. The predictions of the ice volumes are obtained without further processing, while the PCs for

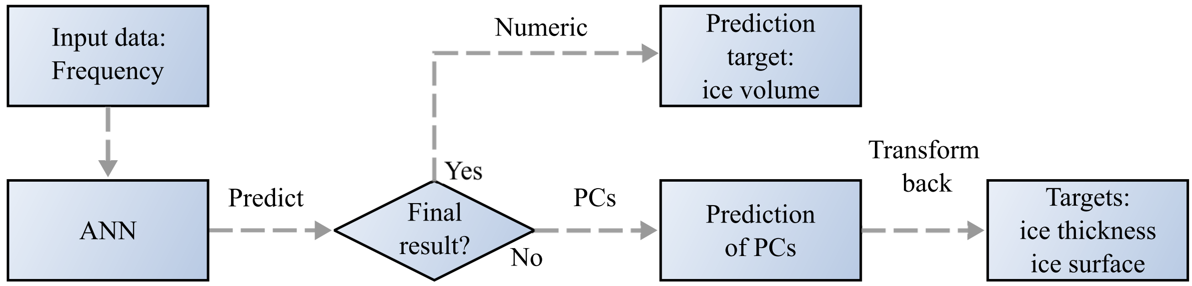

Figure 13: Flowchart of the data streams to predict the targets ice volume and ice thickness.

the ice thickness must be transformed back to the original dimensions of the data. For each prediction target of the ice thickness and ice volume, a separate fully connected ANN is trained. This ANN consists of one input layer, multiple hidden layers and one output layer, which are termed dense layers within TensorFlow. Furthermore, an optimization is conducted to obtain hyperparameters, such as the number of neurons, hidden layers, dropout rate, and learning rate for each ANN, shown in Table 5. The hyperparameter set for the optimization is defined so that the number of neurons decreases with increasing numbers of hidden layers. Thus, a bottleneck-like ANN structure can be achieved. Between each hidden layer and before the output layer, a dropout layer is inserted. The dropout layer deactivates randomly, with a specified dropout rate, neurons at each epoch during the training to reduce possibility of overfitting. The output layer is represented by a dense layer, where the number of neurons for input and output layers are specified by the number of PCs for the corresponding features and targets. Therefore, the input layer of all ANNs contains 40 neurons representing the PCs of the frequency response data. The hyperparameters are shown together with other properties of the ANNs in Table 5. Initially, the rectified linear activation function (ReLU) activation

Table 5: Optimized and used hyperparameter parameters of the ANNs.

Entity	ANN Ice thickness	 Ice volume
	Optimized hyperparameters	
Input layer neurons	40	40
Hidden layer neurons	800, 600, 100	840, 420, 240, 120
Output layer neurons	10	3
Dropout rate	0.2	0.3
Learning rate	0.001	0.001
	Parameters	
Activation function	LeakyReLU	LeakyReLU
Optimizer	Adam	Adam
Batch size	64	64
Epochs	304	500

function was used for each hidden layer, but due to the occurrence of a vanishing gradient problem, which hinders the propagation of information throughout the layers, the LeakyReLU activation function is utilized as a solution, preventing the gradient from reaching zero and returning a small gradient instead.

The output layer requires in this regression task no activation function on the neurons. The adaptive

Adam optimizer is used for all ANNs. Since the prediction of the targets is a regression task, the root mean squared error (RMSE) is used as a performance metric and the mean squared error (MSE) as loss function. Furthermore, an early stopping callback function is applied during training, which monitors the validation loss at each epoch to avoid overfitting. If the ANN fails to decrease the validation loss after a specified number of epochs, the training is aborted. Subsequently, the weights at the best-performing epoch during the training are returned. The optimization of the hyperparameters is conducted with a random grid, which randomly chooses hyperparameters from a predefined parameter set.

4.4. *Prediction results and discussion*

The test data consist of shuffled samples from the dataset with a wide variety of samples. The RMSE and the weighted mean absolute percentage error (WMAPE) are used as evaluation metrics across all regression predictions between the test data and the predictions. The RMSE is defined following

$$\mathrm{RMSE} = \sqrt{\frac{1}{n}\sum_{i=1}^{n}(y_i - \hat{y}_i)^2}, \tag{5}$$

where n represents the number of samples, y represents the test data, and $\hat{y}$ the predicted data. The Mean absolute percentage error (MAPE) and WMAPE are defined as follows

$$\mathrm{MAPE} = \frac{1}{n}\sum\left|\frac{y_i - \hat{y}_i}{y_i}\right| \tag{6}$$

and

$$\mathrm{WMAPE} = \frac{\sum_{i=1}^{n} w_i\left|\frac{y_i - \hat{y}_i}{y_i}\right|}{\sum_{i=1}^{n} w_i}, \tag{7}$$

where the associated weights are denoted by w [34].

Ice volume and ice mass

The ANN developed to predict ice volume produces three numerical values representing the accumulated ice for each sub-volume. These predicted sub-volumes are summed to obtain the total ice volume on the blade. To estimate the accumulated ice mass, the predicted ice volume is multiplied by the ice density, determined at the corresponding temperature, as specified in Section 3.5. The predicted ice volumes and ice masses are shown in Figure 14, where every predicted ice volume and ice mass is plotted against the ice volume and mass from the test data. When the predicted values fall below the ideal prediction line, it indicates that the ANN is underestimating, while predictions above the ideal prediction line indicate overestimation. The minor deviations observed between the predicted and ideal results are uniformly distributed across the range of samples. Therefore, the RMSEs and WMAPEs of the prediction results are similar for all ice volumes and ice mass predictions. In scenarios where ice volumes and ice masses prediction approach zero, the scattering around the ideal prediction line does not impact the RMSE. However, this scattering significantly affects the MAPE metric, which is used to quantify a regression performance. Since the MAPE is sensitive to predictions near zero, the WMAPE is employed, using weights from both test data of the ice volume and ice mass. By using the WMAPE with the weights, the effects of scattering around the ideal line can be effectively taken into account, making it a more suitable metric for these particular predictions. The metrics for the prediction results are shown in Table 6.

The overall calculated WMAPE of 5.7 % for the ice volume and ice mass prediction shows high performance, indicating that the trained ANN is capable of accurately predicting ice volumes, and therefore the accumulated ice masses across the blades.

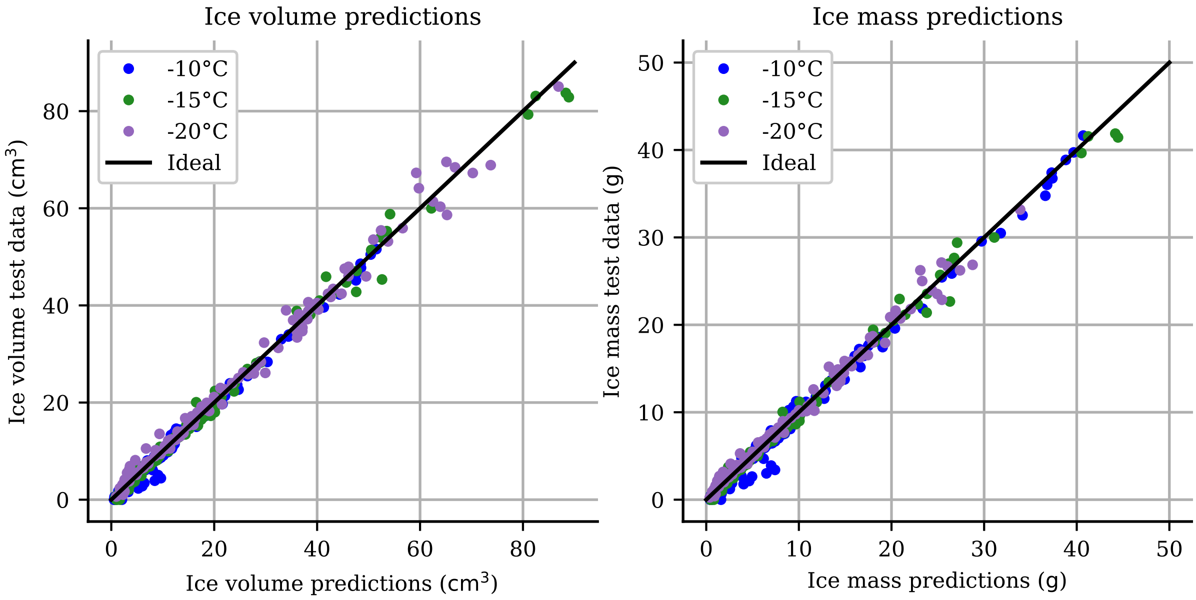

Figure 14: Ice volume and ice mass predictions for each temperature are plotted together with the actual ice volume and ice mass.

Table 6: Prediction results with different metrics for ice sub-volumes and the corresponding ice masses.

Metric	Ice volume				Metric	Ice mass			
	V_1	V_2	V_3	Total		m_1	m_2	m_3	Total
RMSE (cm^3)	0.968	0.978	0.907	1.623	RMSE (g)	0.522	0.427	0.462	0.846
MAPE (%)	14.3	14.6	16.5	16.0	MAPE (%)	14.3	14.6	16.5	16.0
WMAPE (%)	7.6	6.1	6.7	5.7	WMAPE (%)	7.6	6.1	6.7	5.7

Ice thickness

In contrast to ice volume, the ANN is trained to predict ice thickness using 10 PCs. To obtain the actual ice thickness, the PCs are transformed back to the initial data dimensions of 401 data points as demonstrated in Table 4. The results of the ice thickness predictions are illustrated for seven randomly selected test samples in Figure 15. Additionally, the prediction results and the raw measured ice thickness, obtained from the profile laser prior smoothing, are plotted for comparison to each sample. The plotted samples represent various nozzle configurations at different temperatures and stages of ice accumulation. The ANN, trained to predict ice thickness, demonstrates a very high performance, with a RMSE of 0.13 mm and a WMAPE of 5.1 %. The RMSE and WMAPE are calculated by comparing the actual ice thickness values against of the untransformed test data with the predicted ice thickness values from the ANN. Since each prediction consists of 401 data points, the evaluation process involves two steps. First, each prediction sample is evaluated using a WMAPE, with the weight determined by the ice thickness of the test data. In the next step, a WMAPE is taken from all the samples, using the corresponding average ice thicknesses along the blades as weights. Without considering the ice thickness as weights, the MAPE metric over all samples results in 77.9 %, which can not adequately represent the prediction performance for this application. As depicted in Figure 15, the solid line shows that the ANN's predictions closely follow the dotted line representing

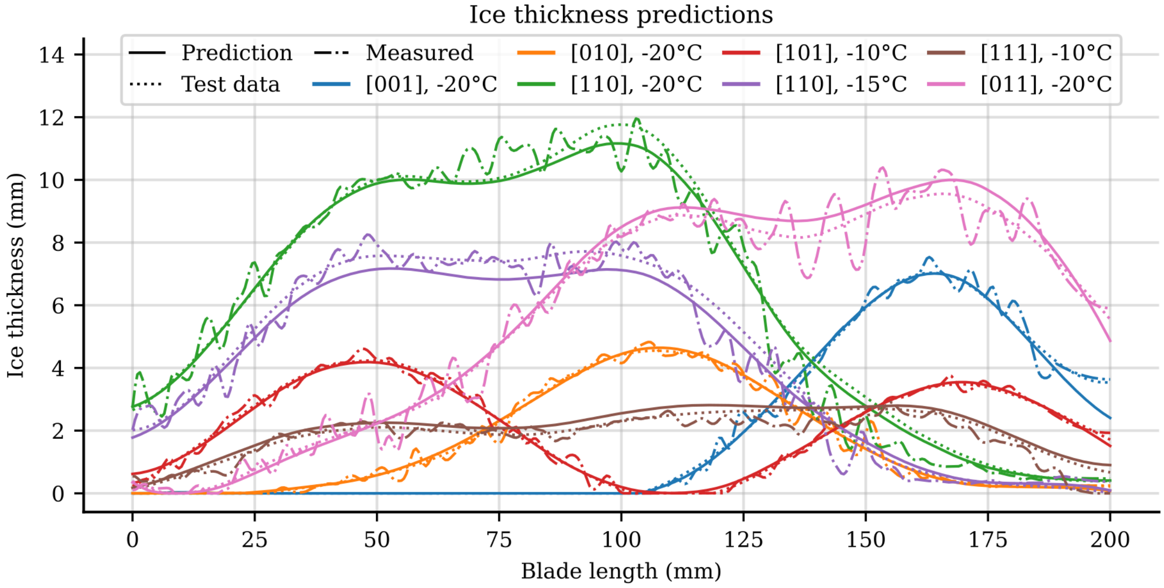

Figure 15: Predicted, actual, and measured ice thicknesses for seven randomly selected test samples are plotted together on the graph. Unique colors represent each sample, with corresponding nozzle configurations and ambient temperatures indicated.

the test data. Together with the low RMSE and WMAPE values, this presents a comprehensive evaluation of the ANN's ability to predict ice thickness on blades under a diverse set of conditions. In conclusion, the data preparation approach, involving smoothing of the ice thickness and application of PCA, has been successfully validated. Moreover, the trained ANN has proven to be capable of predicting the thickness of accumulated ice at the actual location on the blade, based on the frequency response and demonstrated the effectives of the suggested approach.

The application of ANNs to predict the ice proprieties based on the blade's frequency response has some limitations. Despite having the same layup of the manufactured GFRP blades, the frequency responses of the blades clearly differ from one another. The composites blades are made to a high degree of manual labor, which can lead to greater variations in frequency responses. Furthermore, the performance of the ANN relies on the data quality of the dataset.

5. Conclusion

In conclusion, the primary objective of this study was to conduct a comprehensive examination of ice prediction on rotor blades based on their frequency response. Two manufactured rotor blades are equipped each with one vibration-inducing actuator and one accelerometer for response measurements. Frequency responses are obtained using EMAs, actuated with a chirp signal, and then measured by an accelerometer. The icing experiments are carried out employing seven different nozzle configurations and three temperature settings for gathering data in a variety of environmental conditions. Key findings include the distinct influence of ice mass, location, and ambient temperature on the blade's frequency response. Notably, the ANNs demonstrated high performance in predicting ice volume and mass, and even higher performance in predicting ice thickness. The following primary conclusions drawn from the results throughout the investigation:

1. Ice mass, location, and ambient temperature have characteristic impacts on the frequency response of the blade, inducing characteristic shifts and changes in eigenfrequencies.

2. The ANN trained to predict ice volume and mass, with a low WMAPE of 5.7 %, demonstrated high performance.
3. The ANN trained to predict ice thickness demonstrated exceptional performance, resulting in a low WMAPE of 5.1 %, which shows that the ANN is able to accurately predict the ice distribution along the blade.
4. The methodology of predicting ice thickness and distribution across blades has been successfully demonstrated.

It is presumed that the performance of the ANNs would decline when applied to similarly manufactured blades with frequency responses not present within the dataset. Consequently, the applicability of the trained ANN is not easily scalable to comparable blades that exhibit significantly different frequency responses. Therefore, further research is necessary to propose a more generalized model. In addition, scaling this proposed approach to larger WTs entails challenges of data acquisition, which have to be considered.

Data Availability

The supporting data for this research can be obtained from the corresponding author with a justified request.

CRediT authorship contribution statement

Jan Wittig: Methodology, Software, Conceptualization, Validation, Formal analysis, Investigation, Visualization, Writing - original draft. **Georgios Tzortzinis:** Supervision, Resources, Writing - review & editing. **Niels Modler:** Supervision, Resources. **Angelos Filippatos:** Methodology, Conceptualization, Supervision, Resources, Writing - review & editing.

Declaration of Competing Interest

The authors declare that they have no known competing financial interests or personal relationships that could have appeared to influence the work reported in this paper.

References

[1] S. Dale, bp statistical review of world energy 2022 (2022).

[2] L. Shu, H. Li, Q. Hu, X. Jiang, G. Qiu, G. McClure, H. Yang, Study of ice accretion feature and power characteristics of wind turbines at natural icing environment, Cold Regions Science and Technology 147 (2018). doi:https://doi.org/10.1016/j.coldregions.2018.01.006.

[3] L. T. Contreras Montoya, S. Lain, A. Ilinca, A review on the estimation of power loss due to icing in wind turbines, Energies 15 (3) (2022). doi:10.3390/en15031083.

[4] L. Gao, H. Hu, Wind turbine icing characteristics and icing-induced power losses to utility-scale wind turbines, Proceedings of the National Academy of Sciences 118 (42) (2021). doi:10.1073/pnas.2111461118.

[5] Afzal, Faizan, Virk, Muhammad S., Review of icing effects on wind turbine in cold regions, E3S Web Conf. 72 (2018). doi:10.1051/e3sconf/20187201007.

[6] F. Li, H. Cui, H. Su, Iderchuluun, Z. Ma, Y. Zhu, Y. Zhang, Icing condition prediction of wind turbine blade by using artificial neural network based on modal frequency, Cold Regions Science and Technology 194 (2022). doi:https://doi.org/10.1016/j.coldregions.2021.103467.

[7] S. Gantasala, J.-C. Luneno, J.-O. Aidanpää, Investigating how an artificial neural network model can be used to detect added mass on a non-rotating beam using its natural frequencies: A possible application for wind turbine blade ice detection, Energies 10 (2) (2017). doi:10.3390/en10020184.

[8] S. Gantasala, J.-C. Luneno, J.-O. Aidanpää, Identification of ice mass accumulated on wind turbine blades using its natural frequencies, Wind Engineering 42 (1) (2018) 66–84. doi:10.1177/0309524X17723207.
[9] B. Wölfel, Reliable ice detection for rotor blades to increase availability and yield of wind turbines, in: Winterwind, Conference Organization, Åre, Sweden, 2016.
[10] A. Filippatos, S. Schwab, G. Tzortzinis, E. Madia, habil. Maik Gude, In-situ identification of ice accumulation profile and vibration response at composite blades under various icing conditions, Journal of Physics: Conference Series 2526 (1) (2023). doi:10.1088/1742-6596/2526/1/012068.
[11] A. Filippatos, M. Dannemann, M. Nguyen, D. Brenner, M. Gude, Influence of ice accumulation on the structural dynamic behaviour of composite rotors, Applied Sciences 10 (15) (2020). doi:10.3390/app10155063.
[12] N. Modler, A. Winkler, A. Filippatos, D. Weck, M. Dannemann, Function-integrative lightweight engineering – design methods and applications, Chemie Ingenieur Technik 92 (7) (2020). doi:https://doi.org/10.1002/cite.202000010.
[13] Interglas, GLASS FILAMENT FABRICS for PLASTICS REINFORCEMENT PRODUCT SPECIFICATION (2014).
[14] HEXION, EPIKOTE™ Resin MGS™ RIMR 135 and EPIKURE™ Curing Agent MGS™ RIMH 134–RIMH 137 (2006).
[15] H. Schürmann, Konstruieren mit Faser-Kunststoff-Verbunden mit 39 Tabellen, 2nd Edition, Springer, Berlin, 2007.
[16] Extrudr (FD3D GmbH), TECHNICAL DATA SHEET GreenTEC Pro (2020).
[17] R. T. L. Ferreira, I. C. Amatte, T. A. Dutra, D. Bürger, Experimental characterization and micrography of 3d printed pla and pla reinforced with short carbon fibers, Composites Part B: Engineering 124 (2017). doi:https://doi.org/10.1016/j.compositesb.2017.05.013.
[18] ANALOG DEVICES, ADXL321 (2007).
[19] SENSIRION, Datasheet SHT3x-ARP (2016).
[20] L. Tan, J. Jiang, Digital Signal Processing: Fundamentals and Applications, 2nd Edition, Academic Press, Inc., USA, 2013.
[21] C. B. Sullivan, A. Kaszynski, PyVista: 3d plotting and mesh analysis through a streamlined interface for the visualization toolkit (VTK), Journal of Open Source Software 4 (37) (2019) 1450. doi:10.21105/joss.01450.
[22] H. Xue, H. Khawaja, Review of the phenomenon of ice shedding from wind turbine blades, The International Journal of Multiphysics 10 (2016) 265–276. doi:10.21152/1750-9548.10.3.265.
[23] S. Kumarasamy, M. S. Z. Abidin, M. N. A. Bakar, M. Nazida, Z. Mustafa, A. Anjang, Effects of high and low temperature on the tensile strength of glass fiber reinforced polymer composites, IOP Conference Series: Materials Science and Engineering 370 (2018) 012021. doi:10.1088/1757-899x/370/1/012021.
[24] M. Colakoglu, Effect of temperature on frequency and damping properties of polymer matrix composites, Advanced Composite Materials 17 (2) (2008) 111–124. doi:10.1163/156855108X314751.
[25] Pandas development team, pandas-dev/pandas: Pandas (2020). doi:10.5281/zenodo.3509134.
URL https://doi.org/10.5281/zenodo.3509134
[26] P. Schober, C. Boer, L. Schwarte, Correlation coefficients: Appropriate use and interpretation, Anesthesia & Analgesia 126 (2018) 1763–1768. doi:10.1213/ANE.0000000000002864.
[27] V. Scholz, P. Winkler, A. Hornig, M. Gude, A. Filippatos, Structural damage identification of composite rotors based on fully connected neural networks and convolutional neural networks, Sensors 21 (2021) 1–15. doi:10.3390/s21062005.
[28] J. Lever, M. Krzywinski, N. Altman, Principal component analysis, Nature Methods 14 (2017) 641–642. doi:https://doi.org/10.1038/nmeth.4346.
[29] F. Pedregosa, G. Varoquaux, A. Gramfort, V. Michel, B. Thirion, O. Grisel, M. Blondel, et al., Scikit-learn: Machine learning in Python, Journal of Machine Learning Research 12 (2011) 2825–2830.
[30] P. Virtanen, R. Gommers, T. E. Oliphant, M. Haberland, T. Reddy, D. Cournapeau, E. Burovski, et al., SciPy 1.0: Fundamental Algorithms for Scientific Computing in Python, Nature Methods 17 (2020) 261–272. doi:10.1038/s41592-019-0686-2.
[31] C. Peng, J. He, H. Chi, X. Yuan, X. Deng, Icing prediction of fan blade based on a hybrid model, International Journal of Performability Engineering 15 (11) (2019). doi:10.23940/ijpe.19.11.p6.28822890.
[32] L. Chen, G. Xu, L. Liang, Q. Zhang, S. Zhang, Learning deep representation for blades icing fault detection of wind turbines, in: 2018 IEEE International Conference on Prognostics and Health Management (ICPHM), 2018. doi:10.1109/ICPHM.2018.8448394.
[33] M. Abadi, A. Agarwal, P. Barham, E. Brevdo, Z. Chen, C. Citro, G. S. Corrado, et al., TensorFlow: Large-scale machine learning on heterogeneous systems, software available from tensorflow.org (2015).
URL https://www.tensorflow.org/
[34] M. Naser, A. H. Alavi, Error metrics and performance fitness indicators for artificial intelligence and machine learning in engineering and sciences, Architecture, Structures and Construction (2021) 1–19doi:doi.org/10.1007/s44150-021-00015-8.